

Detection and Spatiotemporal analysis of *in-vitro* 3D migratory Triple-Negative Breast cancer cells

Nikolaos M. Dimitriou^{1*}, Salvador Flores-Torres¹, Joseph Matthew Kinsella¹,
Georgios D. Mitsis^{1**}

affiliations: ¹Department of Bioengineering, McGill University, Montreal, QC, H3A 0E9,
Canada.

correspondence: e-mail: * nikolaos.dimitriou@mail.mcgill.ca, ** georgios.mitsis@mcgill.ca

availability: Raw data¹, Code for Image processing², and Spatial analysis³

Abstract

The invasion of cancer cells into the surrounding tissues is one of the hallmarks of cancer. However, a precise quantitative understanding of the spatiotemporal patterns of cancer cell migration and invasion still remains elusive. A promising approach to investigate these patterns are 3D cell cultures, which provide more realistic models of cancer growth compared to conventional 2D monolayers. Quantifying the spatial distribution of cells in these 3D cultures yields great promise for understanding the spatiotemporal progression of cancer. In the present study, we present an image processing and segmentation pipeline for the detection of 3D GFP-fluorescent Triple-Negative Breast Cancer cell nuclei, and we perform quantitative analysis of the formed spatial patterns and their temporal evolution. The performance of the proposed pipeline

¹<https://figshare.com/projects/3D-GROWTH-MDA-MB-231-SERIES-12/118989>

²<https://github.com/NMDimitriou/3D-Preprocessing-Nuclei-Segmentation.git>

³<https://github.com/NMDimitriou/3D-spatial-analysis-cell-nuclei.git>

19 was evaluated using experimental 3D cell culture data, and was found to be com-
20 parable to manual segmentation, outperforming four alternative automated methods.
21 The spatiotemporal statistical analysis of the detected distributions of nuclei revealed
22 transient, non-random spatial distributions that consisted of clustered patterns across
23 a wide range of neighbourhood distances, as well as dispersion for larger distances.
24 Overall, the implementation of the proposed framework revealed the spatial organiza-
25 tion of cellular nuclei with improved accuracy, providing insights into the 3 dimensional
26 inter-cellular organization and its progression through time.

27 **keywords:** Cell segmentation, Point Pattern analysis, Confocal microscopy, 3D cell
28 cultures

29 1 Introduction

30 An important aspect of cancer progression is the migration of cancer cells to the surrounding
31 tissues. Both *in-vivo* and *in-vitro* studies on cancer cell migration have shown that cancers
32 can exhibit several types of patterns including single cell migration, multicellular streaming
33 and collective cell migration, as well as passive patterns, such as tissue folding, and expan-
34 sive growth.¹² Some of these patterns are found in invasive tumours such as breast cancer.
35 Previous studies have shown that the tumour border of breast cancers is dominated by col-
36 lective cell migration forming small acinar structures.¹² Evidence of multicellular streaming
37 also exist from orthotopic breast cancer in xenograft mouse models.²⁶ Other clinical studies
38 on the morphology of the surface of infiltrating ductal adenocarcinoma have shown that the
39 fractal dimension of cancerous tissue is larger compared to normal breast tissue.²¹ Despite
40 the fact that a significant amount of knowledge has been recently obtained for the qualitative
41 characteristics of cancer invasion both *in-vivo* and *in-vitro*, there is still incomplete informa-
42 tion regarding the quantitative characterization of cancer progression, and the investigation
43 of the tumour organization.

44 To this end, 3D cell culture models have become a very promising experimental tool.

45 The main reasons are the increased control of the experimental conditions, the flexibility of
46 data collection compared to *in-vivo* experiments, and their more realistic representation of
47 tumour progression compared to 2D cultures. Differences between 3D and 2D cultures have
48 been observed in cancer growth and its related biochemical processes, such as the secretion
49 of extracellular matrix (ECM) components, and intercellular interaction components¹⁵ while
50 the histological and molecular features of *in-vitro* 3D spheroids exhibit more similarities with
51 xenografts than the conventional 2D monolayers.¹⁵ Another advantage of 3D cell culture
52 models is their flexibility with regards to incorporating more than one cell populations,
53 such as stromal cells, as well as on changing the stiffness of the ECM. The heterotypic
54 intercellular interactions between cancer cells and stromal cells, such as fibroblasts, results
55 in altered cancer cell proliferation and migration, as well as the formation of more compact
56 spheroids compared to equivalent 3D cell mono-culture systems.¹⁵ Additionally, the collection
57 of imaging data for *in-vitro* 3D cell cultures is generally easier and more accurate than *in-vivo*
58 models. Intravital imaging is a common way of data collection for *in-vivo* models; however,
59 this technique suffers from technical challenges such as passive drift of cells or tissues, low
60 penetration depth, tissue heating, and limitations on imaging intervals.¹² On the other hand,
61 confocal microscopy used for *in-vitro* 3D cell cultures can produce higher resolution images,
62 and the data collection intervals are more flexible. Although, 3D cell cultures cannot yet
63 capture the full complexity of tumour growth in a living tissue, overall they have a lot to
64 offer as they provide the opportunity to track even single cells.

65 Confocal microscopy of fluorescent cells, and cell segmentation algorithms are two im-
66 portant tools for the study of 3D *in-vitro* cancer growth. However, some common technical
67 issues related to these two techniques may limit the tracking ability of cancer progression.
68 Increased autofluorescence from out-of-focus cells, and variations in fluorescent signal inten-
69 sity among the cells may pose challenges to cell segmentation algorithms resulting in over-
70 or under-segmentation of cells.¹¹ At the same time, the problem of image segmentation is
71 ill-posed, and up to now there are no algorithms that can be considered as a gold standard.
72 Some key algorithms developed for this purpose are intensity-²³, boundary-³⁵, region-based

73 and region-growing.²⁴ However, they present limitations on the distinction of individual cells
74 in cases of uneven illumination, and in cases where the cells are in contact.

75 To account for this, algorithms that combine multiple methods have been proposed, thus
76 improving the segmentation performance.^{19,32} Watershed segmentation algorithms have be-
77 come popular due to their capability to separate touching cells by utilizing information from
78 their geodesic distance maps, even though they are prone to over-segmentation.³¹ Several
79 variants of the watershed segmentation that address this issue have been proposed, with
80 the marker controlled or seed based watershed transformation being the most popular.²⁸
81 The separation of fused cells has also been approached with concavity-based techniques,
82 which search for the optimal path between two concave points and separate the cells un-
83 der the assumption that their fused shape contains concavities.³³ More sophisticated energy
84 minimization techniques¹⁶ have also been developed; however, their application to datasets
85 containing a large amount of cells can be computationally prohibitive. Novel machine learn-
86 ing based methods exhibit improved performance, however their applicability may be limited
87 to specific datasets, and their performance may be decreased in datasets with high cell shape
88 and volume heterogeneity, as well as high cell density.²⁰ Recent studies have mainly focused
89 on the preprocessing of 3D image stacks, to improve the segmentation results of simpler
90 segmentation algorithms, and are applicable to large datasets.²⁰ Concluding, the advances
91 made in both experimental and image processing methods provide us with the opportunity
92 to further investigate the spatiotemporal organization and progression of cells in greater
93 detail using 3D cell cultures.

94 [Figure 1 about here.]

95 Even though technological advances have provided us appropriate tools for a detailed
96 and quantitative study of spatiotemporal cancer progression, our knowledge so far is rather
97 limited to mostly qualitative aspects of this progression. The possibility of interpreting
98 a cell as a point in the 3D space allows more quantitative, spatial statistical techniques
99 to be employed.¹⁴ Spatial statistical techniques including the Complete Spatial Randomness
100 (CSR) test¹⁰, the characterization of cell distributions using their Inter-Cellular and Nearest-

101 Neighbour distances, and the analysis of cellular density profiles have already been applied
102 for the investigation of tumour morphology and heterogeneity in histology images⁷, the
103 whole-cell dynamic organization of lysosomes¹, as well as the investigation of cell clustering
104 and the correlation the genomic profile of tumours from tissue slices.³⁴

105 In this context, we present a processing, segmentation, and spatiotemporal analysis
106 pipeline for the detection of *in-vitro* 3D cultured fluorescent cancer cells and investigation
107 of their spatiotemporal progression. The proposed pipeline, presented in Fig. 1, utilizes
108 a combination of preprocessing and segmentation algorithms to improve the detection per-
109 formance of GFP-fluorescent nuclei of Triple Negative Breast Cancer (TNBC) cells. The
110 performance of the proposed pipeline was evaluated against manual segmentation, and four
111 alternative pipelines including established⁸, and novel machine learning algorithms.^{20,30} The
112 segmented nuclei were subsequently used for the investigation of their spatiotemporal pro-
113 gression using point-pattern analysis, and density analysis methods. The novel combination
114 of these methods enabled us to detect the position of the cells in the 3D space with higher
115 accuracy, as well as to examine the organization and progression of cancer growth.

116 2 Materials and Methods

117 2.1 Experiments

118 2.1.1 Cell preparation

119 TNBC cells from the MDA-MB-231 cell line with nuclear GFP (histone transfection), were
120 thawed and cultured at 5% CO₂, 37 °C in DMEM (Gibco) at pH 7.2 supplemented with 10%
121 fetal bovine serum (Wisent Bioproducts), 100 U/mL penicillin, 100 µg/mL streptomycin, and
122 0.25 µg/mL, and amphotericin B (Sigma) in T-75 flasks (Corning). The cells were passaged
123 before reaching 85% confluence. Three passages were performed before the 3D cultures; cells
124 were rinsed twice with DPBS and trypsin-EDTA (0.25%-1X, Gibco) was used to harvest
125 them.

126 2.1.2 3D cell cultures

127 A cell-Matrigel (Corning) suspension was created using 0.25 mL of Matrigel (4 °C) and
128 5×10^4 MDA-MB-231/GFP cells. Droplets of 5 μ L cell-Matrigel mixture were manually
129 deposited onto a high performance #1.5 glass bottom 6-well plate (Fisher Scientific). Data
130 acquisition was performed using a confocal microscope (Nikon A1R HD25) coupled with a
131 cell-culture chamber every 2-3 days for a total of 15 days. The dimensions of the 3D cultures
132 were approximately 2500 x 2500 x 900 μ m³. Cell localization was made possible by the GFP
133 fluorophore that is present in cell nuclei (supplementary Fig. S.1). For this study 12 datasets
134 were produced with samples from days 0, 2, 5, 7, 12, 14 each.

135 2.2 Image preprocessing

136 2.2.1 Denoising

Poisson-noise is commonly found in low intensity fluorescent microscopy images.¹⁷ The selected denoising method was the *Poisson Unbiased Risk Estimation-Linear Expansion of Thresholds* (PURE-LET) technique implemented on ImageJ.^{17,27} This method is based on; 1) the search of the closest possible noise-free signal by minimizing the unbiased estimate of the mean squared error (MSE) between the noise-free signal estimates and the noisy signal, 2) the linearity of the estimates, and 3) the use of interscale predictors for the denoising process. The method utilizes a mixed Poisson-Gaussian noise model of the following form

$$y \sim \alpha P(x) + N(\delta, \sigma^2) \quad (1)$$

137 where y is the noisy input data, x the noise-free data, $P(x)$ the Poisson-corrupted input
138 data, α the detector gain, δ the detector offset, and σ the standard deviation of the additive
139 white Gaussian noise. The estimation of the noise parameters (α, δ, σ) is fully automated.

140 2.2.2 Intensity attenuation correction

Confocal microscopy image stacks are usually accompanied by decreasing intensity effects as the depth of the sample increases. The algorithm selected for the attenuation correction⁴ is

implemented on ImageJ, and assumes a stationary background throughout an image stack and rectifies the average intensity and standard deviation by applying a linear transformation to each image slice according to

$$I_{corrected} = m^* + s^* \frac{I_{initial} - m}{s} \quad (2)$$

141 where m^* and s^* are the background average intensity and standard deviation of the reference
142 slice respectively, and m , s are the background average intensity and standard deviation of
143 the current slice. For each slice, the background is estimated by applying a morphological
144 opening with a flat structuring element of radius equal to the radius of the smallest observed
145 nucleus. The estimated background is then subtracted from the corrected image.

146 **2.2.3 Background subtraction**

147 The background subtraction step during the correction of the attenuated intensity was found
148 to be insufficient, because it subtracts only the local background around the nuclei. To
149 fully eliminate background effects, we performed two additional steps. The first step was
150 the background subtraction using the rolling ball algorithm.²⁹ The rolling ball algorithm
151 calculates a local background value for every pixel by averaging over a large ball surrounding
152 the pixel. Using High-Low Look Up Tables (HiLo LUTs) we examined the background effects,
153 and proceeded to manual thresholding of low intensity values, if these effects persisted. In
154 our dataset this threshold was ~ 20 for 8-bit images, however its selection was performed
155 separately for each image, due to varying intensity distributions across samples.

156 **2.2.4 Interpolation**

157 Our sample consisted of images with resolution 999×999 pixels that corresponded to an
158 area of around 2.5×2.5 mm². A nucleus cross-section may have an approximate area of 130
159 μm^2 , which corresponds to a radius 6.43 μm , under the assumption that the cross-section is
160 circular. This translates to a radius of 2.6 pixels. The small size of the nucleus may pose
161 problems during the segmentation due to the fact the intensity gradients may be very steep

162 and narrow. To account for this, we upsampled 10 times each slice of the image stack using
163 cubic spline interpolation. The interpolation was performed in MATLAB.¹⁸

164 **2.3 Nuclei segmentation**

165 **2.3.1 Foreground segmentation**

166 The interpolated images were then used as the input for the Marker based Watershed seg-
167 mentation algorithm. The foreground objects are marked and segmented, iteratively for
168 each image-slice by performing the following steps (supplementary section 2.1): 1) Contrast-
169 limited adaptive histogram equalization (CLAHE) on the initial interpolated grey-level im-
170 age. 2) Erosion on the CLAHE image using a disk shaped mask of radius 10 pixels. 3)
171 “Opening by reconstruction” on the CLAHE image using the markers of step 2 to identify
172 high-intensity objects in the CLAHE image. 4) Dilation of the reconstructed image of step
173 3 using a disk shaped mask of radius 10 pixels. 5) “Closing by reconstruction” of the com-
174 plement image of step 3 using the complement image of step 4 as marker. 6) Detection of
175 regional maxima in the image of step 5. 7) Binarization of the image of step 5 using a locally
176 adaptive threshold calculated by Bradley’s method.⁶ 8) Closing of the image of step 6 using a
177 disk shaped mask of radius 5 pixels followed by morphological erosion, small object removal
178 (with size less than 10 pixels), and filling of holes. 9) Gradient of the CLAHE image. 10)
179 Imposed minima on the result step 9 using as mask the union of the complement image of
180 step 7 and the image of step 8. 11) Watershed image of 10. The watershed map was then
181 binarized⁶ and filtered to remove potentially small or very large artefacts that persisted.
182 The algorithm was implemented in MATLAB.

183 **2.3.2 Fused Nuclei Separation & Centroid Detection**

184 Fused nuclei usually exhibit overlapping intensity distributions that the Marker-Controlled
185 Watershed transform cannot separate. Instead, their separation can be achieved by taking
186 into account their morphological characteristics. In this step, we performed a classic dis-

187 tance based watershed segmentation on the Euclidean distance map of the nuclei detected
188 by the afore mentioned Marker-Controlled Watershed algorithm. The centroids of the seg-
189 mented nuclei were then detected by tracing the edges of the segmentation masks using a
190 26-connected neighbourhood tracing algorithm implemented in MATLAB.

191 [Figure 2 about here.]

192 2.4 Spatial Analysis

193 2.4.1 Complete Spatial Randomness Test of nucleic distributions

The Complete Spatial Randomness (CSR) test examines whether the observed spatial point patterns can be described by a uniform random distribution.⁹ The CSR test was performed using Ripley’s K -function and the *spatstat*³ package of R.²⁵ The K -function¹⁰ is defined as the ratio between the number of the events, i.e. locations of points, j within a distance t from the event i , over the total number of events N , in the studied volume V ($2.5 \times 2.5 \times 0.9$ mm³)

$$K(t) = \hat{\lambda}^{-1} \sum_i \sum_{j \neq i} I(d_{ij} < t) \quad (3)$$

where $\hat{\lambda} = N/V$ denotes the average density of events, N , in the studied volume V , d_{ij} is the distance between events i and j , t is the search radius and I a decision function

$$I(x) = \begin{cases} 1, & \text{if } x = \text{true} \\ 0, & \text{otherwise} \end{cases} \quad (4)$$

194 The K -function was calculated across all datasets and compared against complete spatial
195 randomness that follows a Poisson process $K(t) = 4\pi t^3/3$ in 3D.¹⁰ Isotropic edge correction
196 was applied in the calculation of the K -function. To assess the uncertainty of the random
197 variable K we produced a CSR envelope by generating 100 random distributions and cal-
198 culating the K -function for each of them. The envelope was created by keeping minimum
199 and maximum values of the resulted K values. A substantial upward separation of the

200 observed K -function from the theoretical random K -function denotes clustered patterns,
201 while a downward separation denotes dispersed patterns respectively. Both separation types
202 suggest non-randomness in the distributions.

203 2.4.2 Characterization of the Nucleic Distributions

204 **Inter-Nucleic (IN) Distance Distributions** The IN Distance Distribution for a given
205 sample was calculated by the pairwise Euclidean distances between all nuclei. Given two
206 nuclei i and j with centroid positions $\mathbf{p}_i = (x_i, y_i, z_i)$ and $\mathbf{p}_j = (x_j, y_j, z_j)$ respectively,
207 their pairwise Euclidean distance is given by $D_{ij} = \sqrt{(x_i - x_j)^2 + (y_i - y_j)^2 + (z_i - z_j)^2}$,
208 $i, j = 1 \dots N$, $i \neq j$ where N the total number of nuclei. The similarity between two IN
209 Distance Distributions of different time-points was estimated using the cosine similarity
210 measure (supplementary section 3).¹³

211 **Nearest-Neighbour (NN) Distance Distributions** The NN Distance Distribution for
212 a given sample was calculated using the distances between the nearest neighbours of the
213 nuclei. The NN distance for a given nucleus i is given by the minimum IN Distance between
214 the nucleus i and all the other nuclei of the sample, such as $D_{NN}^i = \min_{i,j} \{D_{ij}\}$, $j \in [1, N]$,
215 $j \neq i$. Similarly, we used the cosine similarity measure to estimate the similarity between
216 two NN distance distributions from different time-points. The IN, and NN Distances, as well
217 as the similarity tests were computed in MATLAB.

218 2.4.3 Density profiles

219 The CSR test and the characterization of the nucleic distance distributions can provide
220 information on the structure of the spatial nucleic distributions. However, they do not
221 provide sufficient information about the location of these distributions in 3D space. The
222 final step of the spatial analysis was the examination of the regions where clustering takes
223 place. To investigate the density of the nucleic distributions and their corresponding locations
224 in 3D space, we estimated the density profiles of the centroids of the nuclei using the Kernel

225 Density estimation via the Diffusion method.⁵

226 **3 Results**

227 **3.1 Preprocessing, Segmentation, and Assessment of Performance**

228 [Figure 3 about here.]

229 The detection of the fluorescent of TNBC nuclei cultured in 3D Matrigel ECM was
230 performed using the proposed image preprocessing and segmentation pipeline. The prepro-
231 cessing stage consists of denoising, intensity attenuation correction, background subtraction,
232 and image interpolation, while the segmentation stage consists of foreground segmentation,
233 splitting of fused nuclei, and detection of the centroids of the segmented nuclei. The effects
234 of preprocessing and segmentation can be inspected in Fig. 2a-2e and Fig. 2f-2g. In Fig. 2h
235 the segmentation result is then rescaled to the original size of the image.

236 The detected centroids across the 7 time-points, as well as the average and standard
237 deviation of the total number of nuclei across all datasets are depicted in Fig. 3, and
238 supplementary Fig. S.2. The results show a biased movement of the cells towards the
239 bottom of the plate. Furthermore, the cells exhibit a sigmoidal proliferative characteristic
240 with numbers ranging from 1000 to 15000 nuclei.

241 The performance of the proposed preprocessing and segmentation pipeline (FluoDeSeg)
242 was assessed using manual segmentation, by drawing the approximate borders of the nuclei,
243 and compared to the performance of four alternative methods of Nasser et al.²⁰, a CellProfiler
244 pipeline⁸, and two pretrained models (cyto and nuclei) of the Cellpose deep-learning segmen-
245 tation algorithm.³⁰ The segmentation performance was calculated using the accuracy, recall,
246 precision, F1 score, Jaccard index (supplementary section 2.3). Additionally, the number of
247 the segmented nuclei from all methods were also compared. Our method exhibited compa-
248 rable accuracy compared to the manual annotation, and the highest accuracy, precision, F1
249 score, and Jaccard index among the three methods, as depicted in the summarized statistics

250 of Table 1 and supplementary Fig. S3a.

251 [Table 1 about here.]

252 [Figure 4 about here.]

253 3.2 Spatial Analysis

254 For the investigation of the spatial organization of the cells, we performed the CSR test, using
255 Ripley's K -function¹⁰, to examine whether the fluorescent nuclei, are randomly distributed
256 in space. The results depicted in Fig. 5a indicate substantial differences from a uniform
257 random distribution. Specifically, we observe clustering for a wide range of neighbourhood
258 radii, as well as an increasing dispersion for longer distances across all samples, with respect
259 to time.

260 The quantitative characterization of the spatial distribution of the cells was performed
261 using the IN, and the NN Euclidean distance distributions. The IN distance distributions
262 quantify the positioning of the cells relative to one another, while the NN distributions
263 measure the distances between each cell and their nearest neighbouring cell. The resulting
264 IN distance distributions, depicted in Fig. 5b, show that they remain relatively stable across
265 all samples and time, with a characteristic peak distance at ~ 1 mm. The cosine similarity
266 test yielded an average similarity value equal to 0.9946 ± 0.0074 , suggesting high similarity
267 between two IN distance distributions across different time-points. Their similarity remained
268 high across all their time-point intervals as shown in supplementary Fig. S.3c. On the other
269 hand, the NN distance distributions, presented in Fig. 5c, formed initially wide distributions
270 that gradually tended to become narrower around lower neighbourhood radii values with
271 respect to time, across all samples, with a characteristic peak at ~ 15 μm . The average cosine
272 similarity between two NN distance distributions from different time-points was found to be
273 equal to 0.8447 ± 0.1686 . The similarity between two NN distance distributions was found
274 to decrease as a function of the time separation between them, as shown in supplementary
275 Fig. S.3d.

276 For the examination of the regions where clustering takes place, we estimated the density
277 profiles of the centroids, using the Kernel Density Estimation via the Diffusion method⁵.
278 The resulting density profiles, depicted in Fig. 6a-6g, suggest that cells were organized into
279 clusters and these clusters tended to change positions in space with respect to time.

280 [Figure 5 about here.]

281 [Figure 6 about here.]

282 4 Discussion

283 In this study, a novel preprocessing and segmentation pipeline allowed us to examine the
284 quantitative aspects of the spatiotemporal progression of cancer cells grown in cultured
285 3D Matrigel ECM. Based on this experimental setting, a more accurate detection of the
286 fluorescent nuclei was achieved, compared to alternative segmentation methods. The spatial
287 analysis revealed a dynamic behaviour of the detected nuclei across time, forming both
288 clustered and dispersion patterns.

289 The pipeline was able to detect more accurately the fluorescent nuclei compared to the
290 four examined alternative methods, and achieved comparable accuracy to the manual an-
291 notation. Specifically, our method achieved the highest accuracy, precision, F1 score, and
292 Jaccard index score among the four methods (Table 1, supplementary Fig. S.3a). The lower
293 recall score was due to an increased amount of pixels classified as False Negative. This
294 result may be due to the background subtraction, which narrows the intensity distribution
295 around the nuclei, even though the information about the location of the nuclei may not be
296 lost. The comparison of the nuclei count of the five methods against the manual annotation
297 showed that our method exhibited the best performance among all examined methods, with
298 a maximum over-segmentation of around 5%, and a maximum under-segmentation of 14%
299 as compared the nuclei count of the manual annotation (Fig. 4). The pipeline was applied to
300 image stacks with planar resolution of 999×999 pixels that correspond to 2.5×2.5 mm², and
301 a nucleus radius of ~ 2.6 pixels. In most cases, the quality of the image stacks was sufficiently

302 good to visually detect fused nuclei from their cluster. However, a possible decrease of the
303 image resolution would most probably affect the segmentation performance. As a result,
304 it is expected that the configuration of the microscope can have a significant effect on the
305 achieved segmentation performance.

306 The CSR test revealed that the nuclei maintained clustered patterns for a wide range
307 of neighbourhood radii across time and that they exhibited more pronounced dispersion
308 patterns with respect to time (Fig. 5a). The biased movement of the cells towards the bottom
309 may have contributed to the increase of clustering patterns in smaller neighbourhood radii.
310 Even though Ripley's K -function provides a measure of the formed patterns, a limitation of
311 this measure is its insensitivity to different point patterns. Specifically, two different point
312 patterns may result in the same K -function². Thus, further steps had to be performed to
313 extract more information about the formed patterns and their behaviour.

314 To investigate the regions of clustering and dispersion, we estimated the density profiles
315 of the centroids of the nuclei. The results revealed organization of cells into smaller clusters
316 and a dynamic behaviour of them in time with lower clustering regions appearing not only at
317 the edges but also close to the center of the space (Fig. 6a-6g). These results, in combination
318 with the results of the CSR test suggest that dispersed patterns did not only appear at the
319 borders of the space, but also within its inner regions of it. This dynamic behaviour can
320 be interpreted as a possible consequence of the need for balance between adhesiveness and
321 access to nutrients, oxygen. While, it is crucial for cells to stay attached to each other,
322 cell crowding may compromise their survival in the inner core of a cluster, due to limited
323 diffusion of nutrients, oxygen, and accumulation of toxic metabolic waste products. We are
324 currently investigating this behaviour by incorporating mathematical models.

325 The IN distance distributions remained stable across all samples (Fig. 5b), maintaining
326 high similarity for different time-points (supplementary Fig. S.3c), and the NN distances
327 were initially widely distributed, and tended to become more narrow around smaller neigh-
328 bourhood radii across time (Fig. 5c), with a decreasing similarity as the distance between
329 time-points increases (supplementary Fig. S.3d). Although we would expect that the increas-

330 ing reduction of the NN distances of these distributions would destabilize the IN distance
331 distributions, this was not found to be the case. The maintenance of the stability of these
332 distributions can be interpreted as a result of the organization of cells into clusters, the fact
333 that cells tended to concentrate towards the bottom of the space with respect to time, as
334 well as their synchronized division.

335 Concluding, the improved performance of the proposed pipeline compared to alternative
336 methods allowed further quantitative investigation of the spatiotemporal progression of these
337 cells. The employed spatial statistical methods allowed the extraction of information for
338 the behaviour of cells across space and time, and the total tumour organization. Future
339 directions include the application of the proposed framework to the investigation of *in-vitro*
340 models with increased complexity, including the incorporation of stromal cell populations in
341 3D cell cultures, as well as the validation of more sophisticated spatiotemporal mathematical
342 models using 3D cell culture data.

343 **Conflict of Interest**

344 The authors have no conflicts of interest to declare.

345 **Acknowledgment**

346 N. M. D. thanks Stavros Niarchos Foundation (F237055R00), Werner Graupe (F202955R00)
347 and McGill University (90025) for the scholarships. S. F. T. thanks McGill University for
348 the McGill Engineering Doctoral Award (90025) and the FRQNT (291010) for the scholar-
349 ships. This work was supported by Cyprus Research and Innovation Foundation (Project:
350 INTERNATIONAL/OTHER/0118/0018).

References

- 351 1. Ba, Q., G. Raghavan, K. Kiselyov, and G. Yang. Whole-Cell Scale Dynamic Organization
352 of Lysosomes Revealed by Spatial Statistical Analysis. *Cell Reports* 23:3591–3606, 2018.
353
- 354 2. Baddeley, A. J., R. A. Moeed, C. V. Howard, and A. Boyde. Analysis of a Three-
355 Dimensional Point Pattern with Replication. *Journal of the Royal Statistical Society:*
356 *Series C (Applied Statistics)* 42:641–668, 1993.
- 357 3. Baddeley, A. J., R. Turner, and Others. Spatstat: An R package for analyzing spatial
358 point patterns.
- 359 4. Biot, E., E. Crowell, H. Hofte, Y. Maurin, S. Vernhettes, and P. Andrey. A new filter for
360 spot extraction in N-dimensional biological imaging. In: 2008 5th IEEE International
361 Symposium on Biomedical Imaging: From Nano to Macro, pp. 975–978, 2008.
- 362 5. Botev, Z. I., J. F. Grotowski, D. P. Kroese, and Others. Kernel density estimation via
363 diffusion. *The annals of Statistics* 38:2916–2957, 2010.
- 364 6. Bradley, D. and G. Roth. Adaptive Thresholding using the Integral Image. *Journal of*
365 *Graphics Tools* 12:13–21, 2007.
- 366 7. Bull, J. A., P. S. Macklin, T. Quaiser, F. Braun, S. L. Waters, C. W. Pugh, and H. M.
367 Byrne. Combining multiple spatial statistics enhances the description of immune cell
368 localisation within tumours. *Scientific Reports* 10:18624, 2020.
- 369 8. Carpenter, A. E., T. R. Jones, M. R. Lamprecht, C. Clarke, I. H. Kang, O. Friman,
370 D. A. Guertin, J. H. Chang, R. A. Lindquist, J. Moffat, P. Golland, and D. M. Sabatini.
371 CellProfiler: image analysis software for identifying and quantifying cell phenotypes.
372 *Genome Biology* 7:R100, 2006.
- 373 9. de Back, W., T. Zerjatke, and I. Roeder. *Statistical and Mathematical Modeling of*
374 *Spatiotemporal Dynamics of Stem Cells*, pp. 219–243, Springer New York, 2019.

- 375 10. Dixon, P. M. Ripley's K Function. Wiley StatsRef: Statistics Reference Online 3:1796–
376 1803, 2014.
- 377 11. Fatima, M. M. and V. Seenivasagam. A marker controlled watershed algorithm with
378 priori shape information for segmentation of clustered nuclei. International Journal of
379 Advanced Research in Computer Science 2, 2011.
- 380 12. Friedl, P., J. Locker, E. Sahai, and J. E. Segall. Classifying collective cancer cell invasion.
381 Nature Cell Biology 14:777–783, 2012.
- 382 13. Han, J., M. Kamber, and J. Pei. 2 - Getting to Know Your Data. In: The Morgan
383 Kaufmann Series in Data Management Systems, edited by J. Han, M. Kamber, and
384 J. B. T. D. M. T. E. Pei, pp. 39–82, Boston, 2012.
- 385 14. Heindl, A., S. Nawaz, and Y. Yuan. Mapping spatial heterogeneity in the tumor mi-
386 croenvironment: a new era for digital pathology. Laboratory Investigation 95:377–384,
387 2015.
- 388 15. Hickman, J. A., R. Graeser, R. de Hoogt, S. Vidic, C. Brito, M. Gutekunst, H. van der
389 Kuip, and I. M. I. P. Consortium. Three-dimensional models of cancer for pharmacology
390 and cancer cell biology: Capturing tumor complexity in vitro/ex vivo. Biotechnology
391 Journal 9:1115–1128, 2014.
- 392 16. Li, C., C. Xu, C. Gui, and M. D. Fox. Distance Regularized Level Set Evolution and Its
393 Application to Image Segmentation. IEEE Transactions on Image Processing 19:3243–
394 3254, 2010.
- 395 17. Luisier, F., C. Vonesch, T. Blu, and M. Unser. Fast interscale wavelet denoising of
396 Poisson-corrupted images. Signal Processing 90:415–427, 2010.
- 397 18. MATLAB. 9.7.0.1190202 (R2019b), Natick, Massachusetts: The MathWorks Inc. 2018.

- 398 19. Mohammed, J. G. and T. Boudier. Classified region growing for 3D segmentation of
399 packed nuclei. In: 2014 IEEE 11th International Symposium on Biomedical Imaging
400 (ISBI), pp. 842–845. 2014.
- 401 20. Nasser, L. and T. Boudier. A novel generic dictionary-based denoising method for im-
402 proving noisy and densely packed nuclei segmentation in 3D time-lapse fluorescence
403 microscopy images. *Scientific Reports* 9:5654, 2019.
- 404 21. Norton, L. Conceptual and Practical Implications of Breast Tissue Geometry: Toward
405 a More Effective, Less Toxic Therapy. *The Oncologist* 10:370–381, 2005.
- 406 22. Ostertagova, E., O. Ostertag, and J. Kováč. Methodology and application of the Kruskal-
407 Wallis test. In: *Applied Mechanics and Materials*, volume 611, pp. 115–120, Trans Tech
408 Publ, 2014.
- 409 23. Otsu, N. A Threshold Selection Method from Gray-Level Histograms. *IEEE Transactions*
410 *on Systems, Man, and Cybernetics* 9:62–66, 1979.
- 411 24. Prados-Suárez, B., J. Chamorro-Martínez, D. Sánchez, and J. Abad. Region-based fit
412 of color homogeneity measures for fuzzy image segmentation. *Fuzzy Sets and Systems*
413 158:215–229, 2007.
- 414 25. R Core Team. R: A Language and Environment for Statistical Computing [https://www.](https://www.r-project.org/)
415 [r-project.org/](https://www.r-project.org/).
- 416 26. Roussos, E. T., M. Balsamo, S. K. Alford, J. B. Wyckoff, B. Gligorijevic, Y. Wang,
417 M. Pozzuto, R. Stobezki, S. Goswami, J. E. Segall, D. A. Lauffenburger, A. R. Bresnick,
418 F. B. Gertler, and J. S. Condeelis. Mena invasive (MenaINV) promotes multicellular
419 streaming motility and transendothelial migration in a mouse model of breast cancer.
420 *Journal of Cell Science* 124:2120–2131, 2011.
- 421 27. Schindelin, J., I. Arganda-Carreras, E. Frise, V. Kaynig, M. Longair, T. Pietzsch,
422 S. Preibisch, C. Rueden, S. Saalfeld, B. Schmid, J.-Y. Tinevez, D. J. White, V. Harten-

- 423 stein, K. Eliceiri, P. Tomancak, and A. Cardona. Fiji: an open-source platform for
424 biological-image analysis. *Nature Methods* 9:676, 2012.
- 425 28. Schmitt, O. and M. Hasse. Morphological multiscale decomposition of connected regions
426 with emphasis on cell clusters. *Computer Vision and Image Understanding* 113:188–201,
427 2009.
- 428 29. Sternberg, S. R. Biomedical image processing. *Computer* pp. 22–34, 1983.
- 429 30. Stringer, C., T. Wang, M. Michaelos, and M. Pachitariu. Cellpose: a generalist algorithm
430 for cellular segmentation. *Nature Methods* 18:100–106, 2021.
- 431 31. Vincent, L. and P. Soille. Watersheds in digital spaces: an efficient algorithm based on
432 immersion simulations. *IEEE Transactions on Pattern Analysis & Machine Intelligence*
433 pp. 583–598, 1991.
- 434 32. WÄHLBY, C., I.-M. SINTORN, F. ERLANDSSON, G. BORGEFORS, and
435 E. BENGTSSON. Combining intensity, edge and shape information for 2D and 3D
436 segmentation of cell nuclei in tissue sections. *Journal of Microscopy* 215:67–76, 2004.
- 437 33. Wienert, S., D. Heim, K. Saeger, A. Stenzinger, M. Beil, P. Hufnagl, M. Dietel,
438 C. Denkert, and F. Klauschen. Detection and Segmentation of Cell Nuclei in Virtual
439 Microscopy Images: A Minimum-Model Approach. *Scientific Reports* 2:503, 2012.
- 440 34. Yuan, Y., H. Failmezger, O. M. Rueda, H. R. Ali, S. Gräf, S.-F. Chin, R. F. Schwarz,
441 C. Curtis, M. J. Dunning, H. Bardwell, N. Johnson, S. Doyle, G. Turashvili, E. Proven-
442 zano, S. Aparicio, C. Caldas, and F. Markowetz. Quantitative Image Analysis of Cellular
443 Heterogeneity in Breast Tumors Complements Genomic Profiling. *Science Translational*
444 *Medicine* 4:157ra143, 2012.
- 445 35. Ziou, D. and S. Tabbone. *Edge Detection Techniques - An Overview*, volume 8. 2000.

446 List of Figures

447	1	Proposed pipeline for the preprocessing of 3D image stacks, segmentation of fluorescent nuclei, and their spatiotemporal statistical analysis.	21
448			
449	2	Segmentation process for fluorescent nuclei of 3D cell culture model. (2a) Raw image slice found at 80 μm height from the bottom of the well of a cell laden Matrigel dome in the 9th day of the experiment. (2b) Zoomed raw image of the red box region of (2a). (2c) Denoised and background subtraction result resulting from (2b). (2d) Zoomed image of the red box in (2c). (2e) Interpolation result resulting from (2d). (2f) Marker Controlled Watershed segmentation. (2g) Nuclei splitting with Distance Based Watershed segmentation. (2h) Rescaling back to original image size.	22
450			
451			
452			
453			
454			
455			
456			
457	3	(3a)-(3g) Result from the application of the processing and segmentation pipeline in a representative dataset. Title notation $D\#$ refers to the time-point of the image acquisition in days. (3h) Mean and standard deviation for the nuclei count across 12 datasets.	23
458			
459			
460			
461	4	Normalized nuclei counts obtained by the three examined methods with respect to the nuclei count achieved by the manual annotation. Values greater than 1, and less than 1 denote over-segmentation, and under-segmentation, respectively. The results overall suggest that the proposed pipeline exhibits improved performance with respect to all the examined measures, with the exception of the recall score.	24
462			
463			
464			
465			
466			
467	5	(5a) Average values of K -function across all samples and the corresponding standard error of mean (SEM). Upward separation of the observed K -function from the theoretical random K -function denotes clustered patterns, while downward separation denotes dispersed patterns. (5b) Inter-Nucleic Distance Distributions across all samples. (5c) Nearest-Neighbour Distance Distributions across all samples. The title ($D\#$) denotes the time-point in days.	25
468			
469			
470			
471			
472			
473			
474	6	(6a)-(6g) Density profiles of a representative sample across time. The values in the legends indicate the density values of the contours painted with the same colour.	26
475			
476			

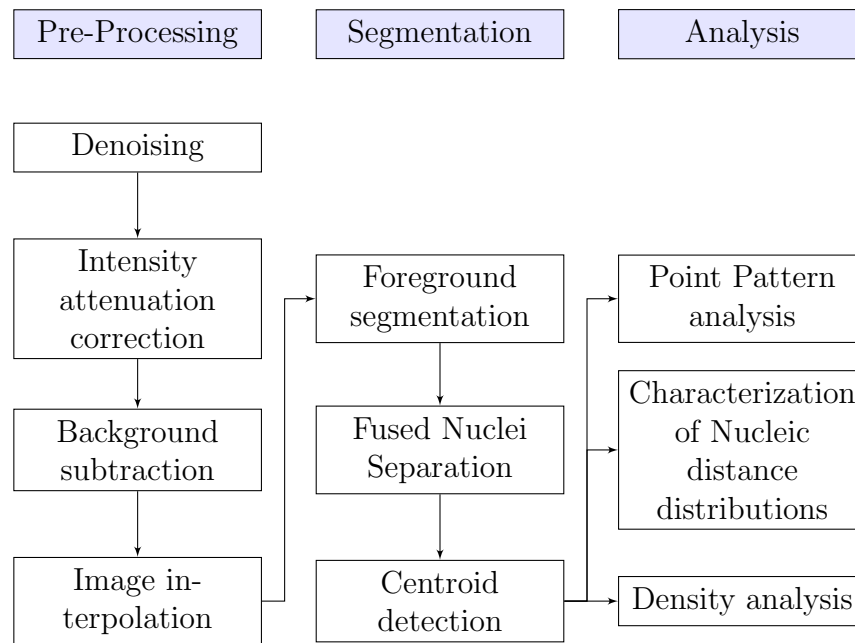


Figure 1: Proposed pipeline for the preprocessing of 3D image stacks, segmentation of fluorescent nuclei, and their spatiotemporal statistical analysis.

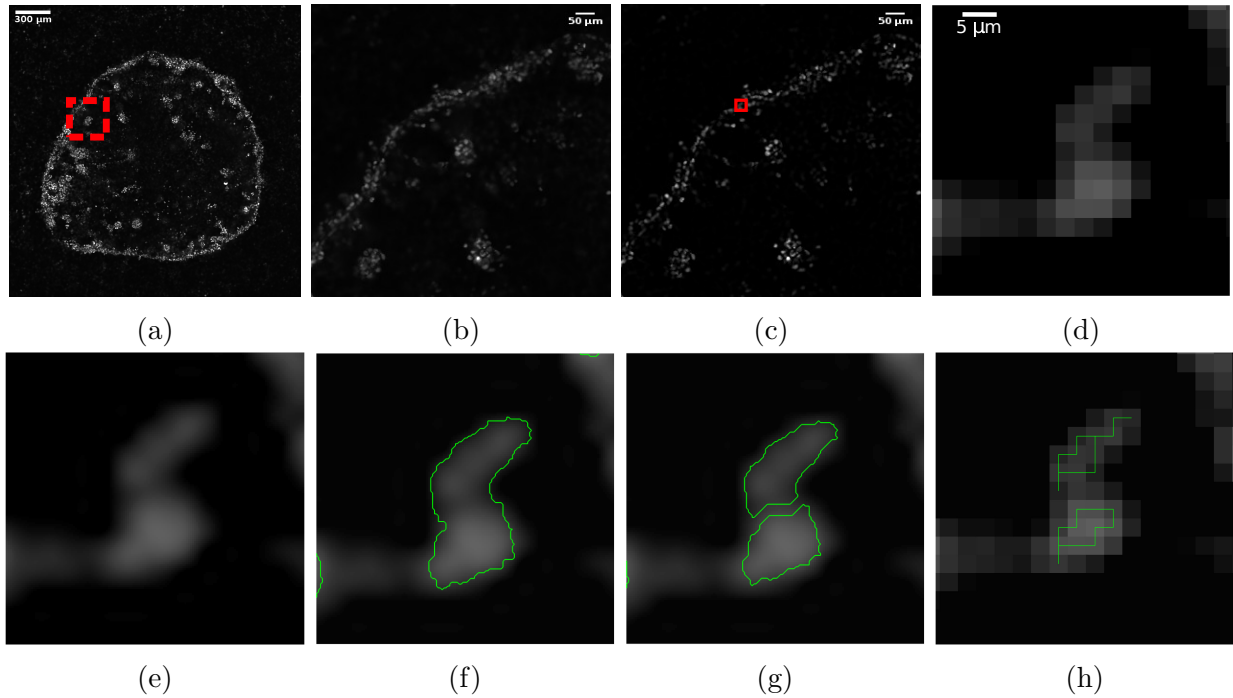


Figure 2: Segmentation process for fluorescent nuclei of 3D cell culture model. (2a) Raw image slice found at 80 μm height from the bottom of the well of a cell laden Matrigel dome in the 9th day of the experiment. (2b) Zoomed raw image of the red box region of (2a). (2c) Denoised and background subtraction result resulting from (2b). (2d) Zoomed image of the red box in (2c). (2e) Interpolation result resulting from (2d). (2f) Marker Controlled Watershed segmentation. (2g) Nuclei splitting with Distance Based Watershed segmentation. (2h) Rescaling back to original image size.

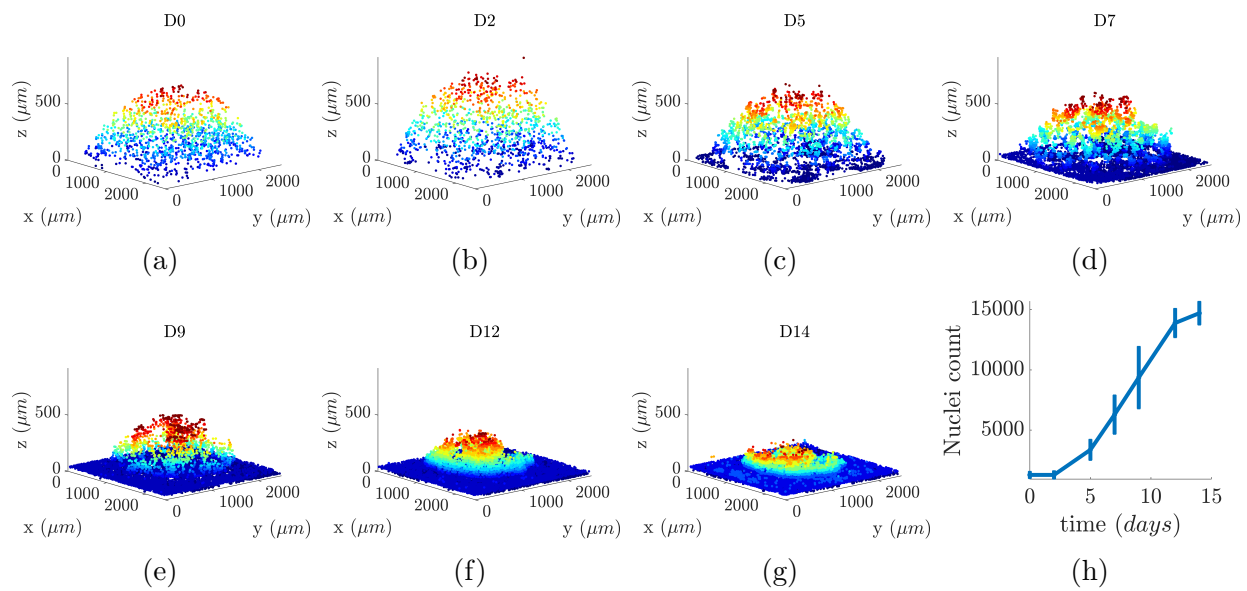


Figure 3: (3a)-(3g) Result from the application of the processing and segmentation pipeline in a representative dataset. Title notation D# refers to the time-point of the image acquisition in days. (3h) Mean and standard deviation for the nuclei count across 12 datasets.

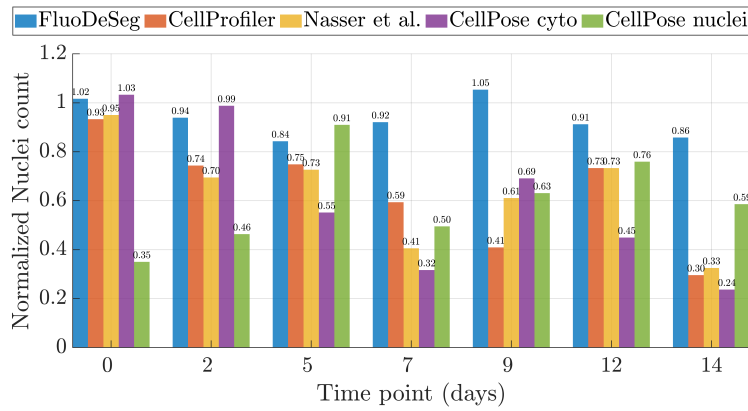


Figure 4: Normalized nuclei counts obtained by the three examined methods with respect to the nuclei count achieved by the manual annotation. Values greater than 1, and less than 1 denote over-segmentation, and under-segmentation, respectively. The results overall suggest that the proposed pipeline exhibits improved performance with respect to all the examined measures, with the exception of the recall score.

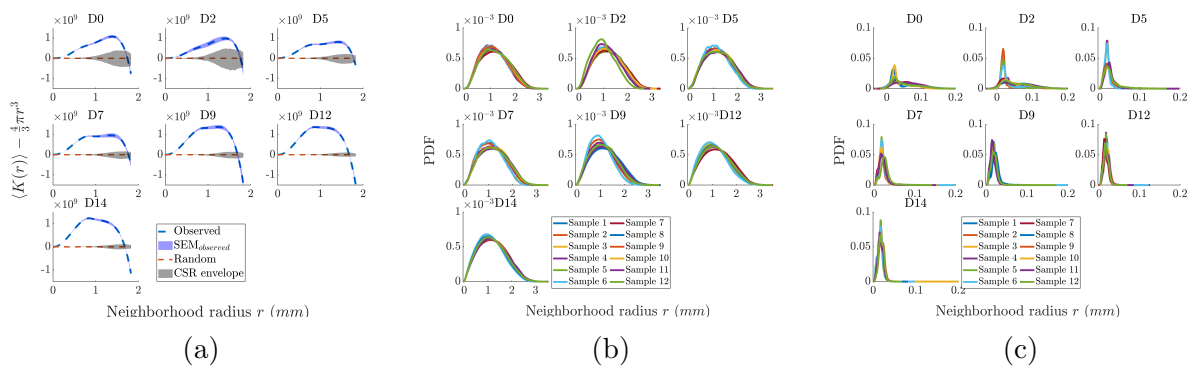


Figure 5: (5a) Average values of K -function across all samples and the corresponding standard error of mean (SEM). Upward separation of the observed K -function from the theoretical random K -function denotes clustered patterns, while downward separation denotes dispersed patterns. (5b) Inter-Nucleic Distance Distributions across all samples. (5c) Nearest-Neighbour Distance Distributions across all samples. The title (D#) denotes the time-point in days.

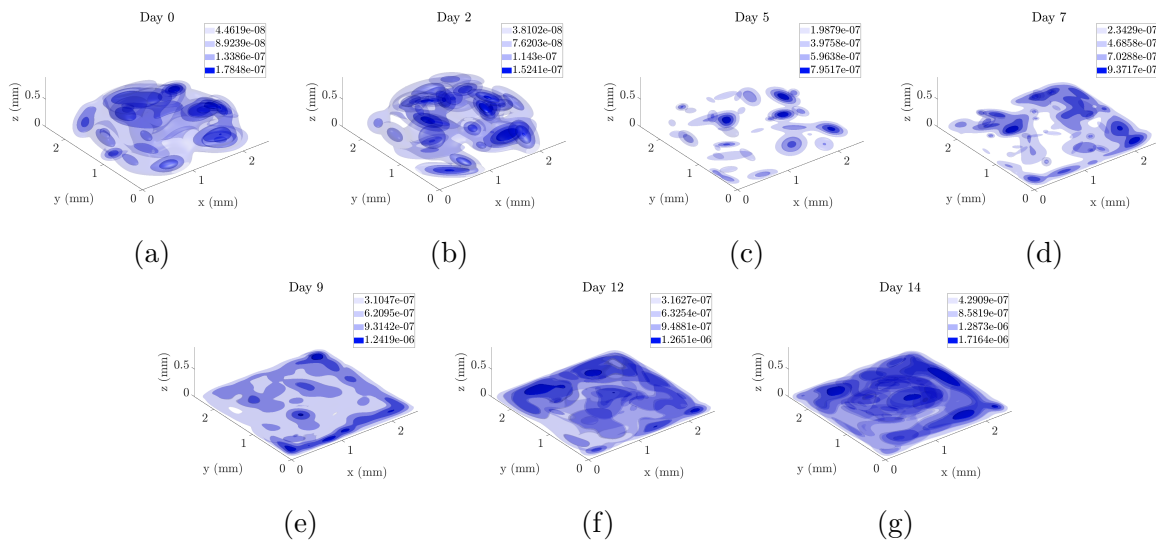


Figure 6: (6a)-(6g) Density profiles of a representative sample across time. The values in the legends indicate the density values of the contours painted with the same colour.

477 List of Tables

478	1	Segmentation performance of the proposed pipeline (FluoDeSeg), the method	
479		developed by Nasser et al. ²⁰ , the CellProfiler pipeline ⁸ , and the two Cellpose	
480		models (cyto and nuclei) ³⁰ as compared to manual segmentation. Results are	
481		reported as Mean \pm Standard Deviation. The symbols *, †, ‡, and ★ denote	
482		p-value < 0.05 for the Kruskal-Wallis test ²² between FluoDeSeg and Nasser et	
483		al., between FluoDeSeg and CellProfiler, FluoDeSeg and Cellpose cyto, and	
484		FluoDeSeg and Cellpose nuclei, respectively.	28

Table 1: Segmentation performance of the proposed pipeline (FluoDeSeg), the method developed by Nasser et al.²⁰, the CellProfiler pipeline⁸, and the two Cellpose models (cyto and nuclei)³⁰ as compared to manual segmentation. Results are reported as Mean \pm Standard Deviation. The symbols *, †, ‡, and ★ denote p-value < 0.05 for the Kruskal-Wallis test²² between FluoDeSeg and Nasser et al., between FluoDeSeg and CellProfiler, FluoDeSeg and Cellpose cyto, and FluoDeSeg and Cellpose nuclei, respectively.

Method	FluoDeSeg	Nasser et al. ²⁰	Cellprofiler ⁸	Cellpose cyto ³⁰	Cellpose nuclei ³⁰
Acuracy ‡	0.978 \pm 0.023	0.914 \pm 0.092	0.959 \pm 0.040	0.913 \pm 0.064	0.969 \pm 0.028
Recall * † ‡	0.642 \pm 0.119	0.895 \pm 0.086	0.828 \pm 0.082	0.883 \pm 0.102	0.445 \pm 0.313
Precision * † ★	0.691 \pm 0.691	0.275 \pm 0.275	0.462 \pm 0.462	0.201 \pm 0.201	0.372 \pm 0.372
F1 * † ★	0.653 \pm 0.109	0.402 \pm 0.127	0.563 \pm 0.203	0.319 \pm 0.081	0.389 \pm 0.194
Jaccard * † ★	0.487 \pm 0.060	0.260 \pm 0.136	0.402 \pm 0.129	0.194 \pm 0.111	0.265 \pm 0.244